Detailed Atomic Reconstruction of Extended Line Defects in Monolayer MoS_2

Shanshan Wang[1], *Gun-Do Lee*[2], *Sungwoo Lee*[2], *Euijoon Yoon,*[2] *Jamie H. Warner*[1] *

[1]Department of Materials, University of Oxford, Parks Road, Oxford, OX1 3PH, United Kingdom

[2]Department of Materials Science and Engineering, Seoul National University, 151-742, Seoul, Korea

*Jamie.warner@materials.ox.ac.uk;

Abstract

We study the detailed bond reconstructions that occur in S vacancies within monolayer MoS_2 using a combination of aberration-corrected transmission electron microscopy, density functional theory and multislice image simulations. Removal of a single S atom causes little perturbation to the surrounding MoS_2 lattice, whereas the loss of two S atoms from the same atomic column causes a measureable local contraction. Aggregation of S vacancies into linear line defects along the zig-zag direction results in larger lattice compression that is more pronounced as the length of the line defect increases. For the case of two rows of S line vacancies we find two different types of S atom reconstruction with different amounts of lattice compression. Increasing the width of line defects leads to nanoscale regions of reconstructed MoS_2 that are shown by DFT to behave as metallic channels. These results provide important insights into how defect structures could be used for creating metallic tracks within semiconducting monolayer MoS_2 films for future applications in electronics and opto-electronics.

KEYWORDS: MoS_2, transition metal dichalcogenides, Aberration-corrected TEM, defects.

Monolayer molybdenum disulphide (MoS_2) is a two-dimensional transition metal dichalcogenides (TMDs) consisting of three hexagonally-arranged S-Mo-S atomic planes. It is a direct band gap semiconductor and is complementary to the semi-metal nature of graphene for expanding 2D materials in the application areas of nanoelectronics, optoelectronics and flexible devices.[1–4] Several different approaches have been utilized to obtain MoS_2 monolayers, including exfoliation,[5] hydrothermal synthesis[6] and chemical vapour deposition (CVD).[7–13] CVD has the greatest potential to produce wafer-scale high-quality monolayer films of TMDs for future industrial needs. Further tuning of the fundamental properties of TMDs can be achieved by doping,[14,15] strain engineering[16,17] and phase transitions.[18] These modify the band gap structure of MoS_2 and can even switch its electronic characteristics from semiconducting to metallic.

Structural imperfections in graphene, such as point defects, dislocations, edges and grain boundaries, can impact its chemical, mechanical, optical and electronic properties. The effects can be beneficial, such as providing active bonding sites for absorbed atoms and molecules in controlled chemical reactions, or detrimental, such as decreasing the charge carrier mobility for graphene-based field-effect transistors.[19,20] There have also been several reports concerning defects in monolayer MoS_2 and the TMDs family in general. For example, a unique class of trefoil-like point defects formed by 60° rotations of metal-chalcogen bonds has been recently discovered, which could give rise to p-type doping and local magnetic moments.[21] In addition, due to the flexibility of coordination characteristics for both transition metal and chalcogen atoms, a variety of grain boundaries composed of a series of dislocation cores having 5|7, 4|4, 4|6, 4|8, and 6|8 fold rings have been discovered. Some of these defect structures are predicted to be one-dimensional conductive channels embedded in the intrinsic trigonal prismatic lattice, providing exciting opportunities to tailor local properties of monolayer MoS_2.[9,22,23] All these examples offer successful paradigms of adjusting monolayer MoS_2 properties through defect engineering.

Electron beam irradiation can create defects in 2D materials, due to either a 'knock-on' effect, ionization or beam-induced chemical etching, facilitating the sculpting of 2D membranes with high spatial accuracy and flexible pattern design.[24,25] A recent study showed that 60° grain boundaries around vacancy-induced inversion domains on TMD monolayers can be generated artificially by a proper dose of electron irradiation.[26] The electron beam in the transmission electron microscope can be utilized not only as an imaging tool but also as a probe for precise nanostructure fabrication. Theoretical calculations reported that the displacement threshold of S atoms in a pristine MoS_2 lattice is ~ 6.5 eV, similar to the maximum knock-on energy transferred from 80 keV electrons to S atoms.[27,28] Therefore, a prolonged electron beam illumination on monolayer MoS_2 under 80kV can produce large amounts of S vacancies. In contrast, bond rotations similar to Stone–Wales defects in graphene, need much higher formation energy and are not favourable in MoS_2 under this imaging condition at room temperature.[21] The isolated S vacancies are prone to agglomerating into line defects of various geometries, which are different from the defect structures produced in graphene.[29,30] Although line defects in transition metal dichalcogenides have been imaged before by AC-TEM, the spatial resolution was not sufficient to accurately resolve the positions of all S atoms within the defect structure and provide direct insights into the detailed S bond lengths and reconstructions.[29] The details of subtle lattice reconstructions in line defects in monolayer MoS_2, such as the bond length changes and S atom positions are needed for precise theoretical predictions of its electronic and magnetic properties.

Here, we use a combination of atomic resolution imaging by aberration corrected TEM (AC-TEM) and DFT calculations to systematically study the lattice reconstructions associated with line defects in MoS_2. We provide detailed information about bond length changes and 2D strain field variations for line defects as a function of their length and width, as well as a prediction on the band structure evolution from semiconducting to metallic as the line defect broadens in width.

Results and Discussion

Monolayer MoS_2 is produced by chemical vapour deposition growth using our previously reported method.[11] Samples are transferred to SiN TEM grids with 2 μm holes using a polymer support layer that is removed to leave suspended monolayer MoS_2 regions. AC-TEM imaging is performed using an accelerating voltage of 80kV, which has sufficient energy to produce S vacancies. Monochromation of the electron beam is used to reduce the effects of chromatic aberration and achieve AC-TEM images with higher spatial resolution than using just spherical aberration correction alone can achieve and this increases the ability to resolve the position of atoms. Single S vacancies (SV) and double S vacancies (DV) are the two simple point defects produced in monolayer MoS_2 under electron beam irradiation, shown in figure 1a-1d.

Bond length measurements in the SV region were obtained using boxed line profiles along three armchair directions starting from one SV site in figure 1e, spanning four atoms in projection as S-Mo-2S-Mo, which is schematically illustrated in figure 1i (supporting information figure S1). The distance between atoms is determined by fitting double Gaussians and measuring the distance between Gaussian peak positions, with the distance scale calibrated by measuring Mo-S bonds in a pristine region of MoS_2 lattice. The distances measured between atoms in the AC-TEM image are the 2D projected distances of MoS_2. The deviations of bond lengths between S-Mo and 2S-Mo in three armchair directions for the SV are almost negligible and are close to the standard 2S-Mo distance measured in 2D projection (~1.8 Å). Small fluctuations in the distance is attributed to the influence of other SVs around the area and are within the noise level of the measurement (labelled by white circles in figure 1e).

For the DV in figure 1f, the loss of two S atoms causes the distance between the three neighbouring Mo atoms to be reduced by 12% from a value of 3.13 Å in the pristine lattice to 2.75, 2.75 and 3.02 Å, (labelled by 1, 2 and 3, respectively), figure 1j. The Mo-Mo bond contraction along three zigzag directions in the DV is not purely isotropic and we attributed this to the random distribution of other SVs around DV (marked by white circles in figure 1f), exerting anisotropic influence on the lattice configuration at the DV site. This effect is supported by the DFT calculations (supporting information figures S2 and S3). In comparison, the Mo-Mo bond lengths around the one missing S atom in the SV were all measured as ~3.10 Å, which is close to the pristine value and indicates negligible compression.

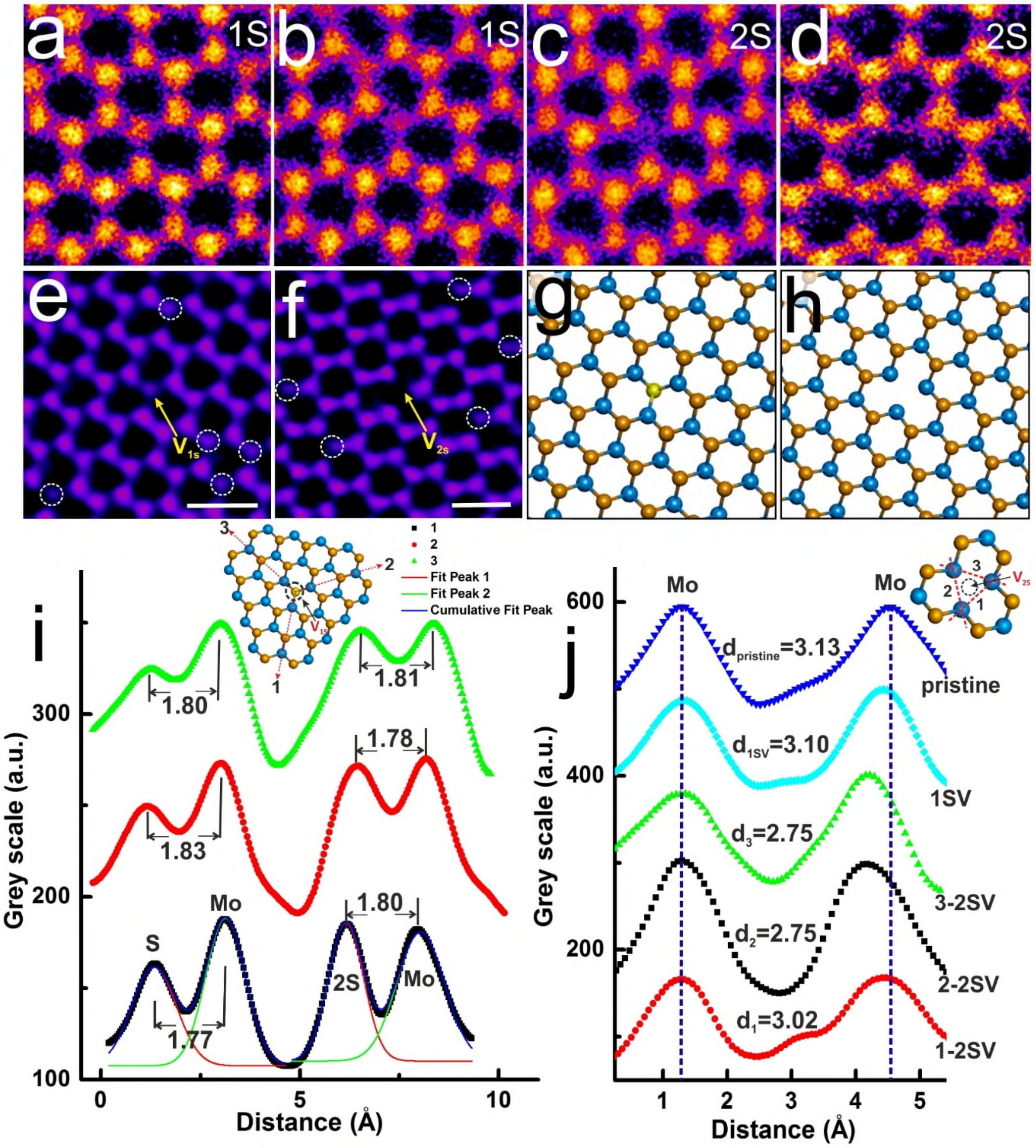

Figure 1. (a, b) Typical AC-TEM images of SV in MoS_2. (c, d) Typical AC-TEM images DV in MoS_2. (e-f) AC-TEM images of SV and DV, represented as V_{1S} and $V_{2S,}$ respectively. The typical examples that are used to conduct bond length measurements in figures 1i and 1j have been highlighted by yellow arrows. The distribution of other single S vacancies around are marked by white circles. (g, h) DFT-calculated atomic models for SV and DV, respectively, in a pristine monolayer MoS_2 lattice. (i, j) Intensity line profiles at SV and DV shown in figure 1e and 1f, respectively, along directions indicated by red arrows in the schematic diagrams in each panel. Scale bar corresponds to 0.5nm in all panels.

Prolonged electron beam irradiation causes the concentration of point defects to increase, with a tendency to initially aggregate into small clusters and then form extended line defect networks (figure 2a to 2c; supporting information figure S4). Figure 2d shows the detailed lattice structure corresponding to the early stage of vacancy agglomeration, where isolated point defects begin to migrate and gather into small clusters and short lines in different geometries, indicated by white circles and lines (supporting information figure S5). As the size of the vacancy cluster grows, the amount of bond reconstruction increases, as shown in the red and yellow circles in figure 2d. The defect clusters primarily adopt linear geometry, which is different to graphene defect clusters at room temperature. These line defects have a certain length along the zig-zag direction determined by the number of missing S atoms, but can also grow across more than one zig-zag lattice line to obtain width in the arm-chair direction. The width of a line defect is essentially the number of adjoining parallel S vacancy lines (n), and denoted as nSVL. Some S point defects agglomerate into ultra-short 1SVL, 2SVL and 3SVL, as shown in figure 2e to 2g, respectively, and become the nucleation of future extended line defects.

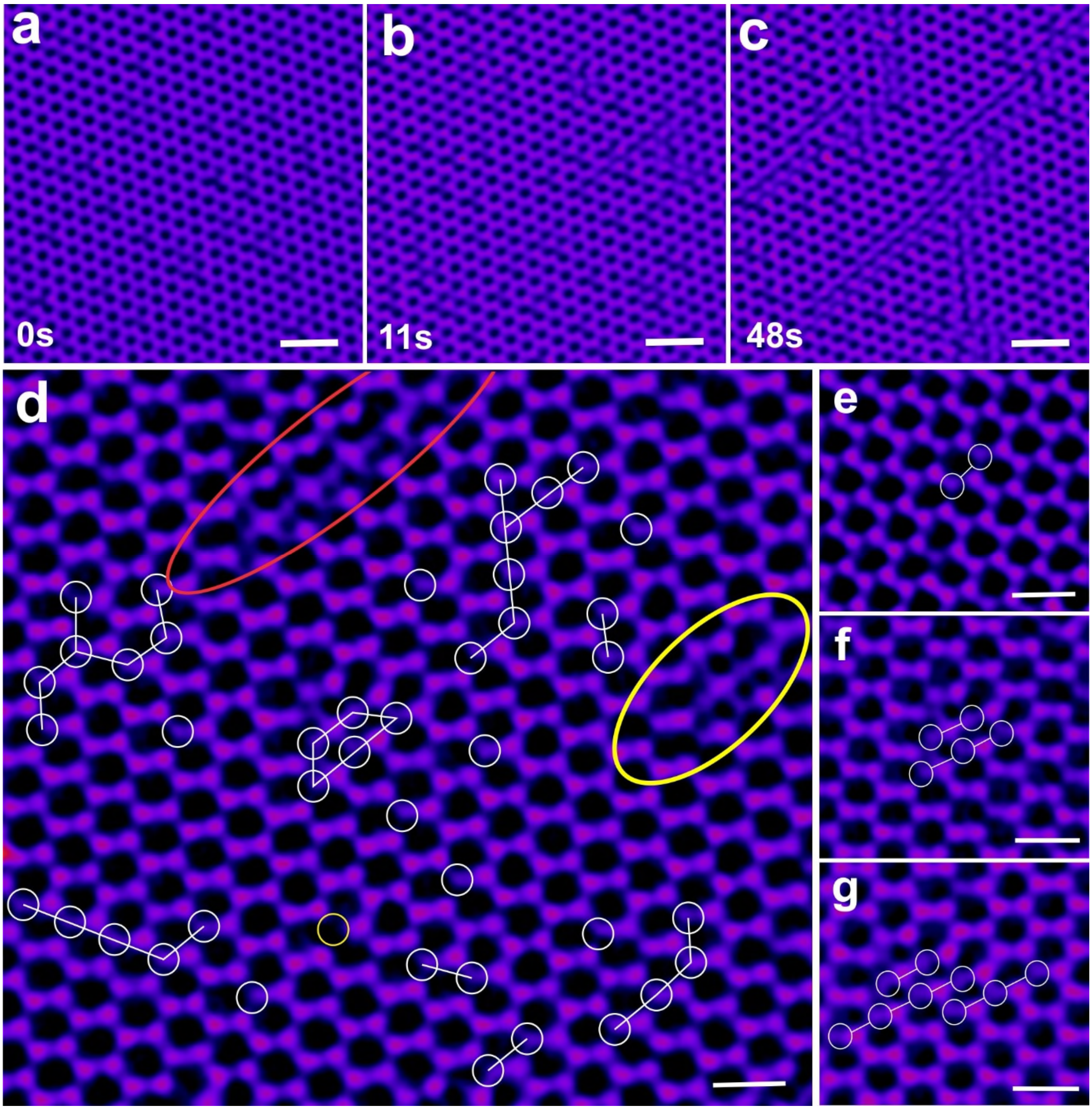

Figure 2. (a-c) Sequence of AC-TEM images showing isolated S vacancies aggregating into extended line defects under a continuous electron beam illumination at an accelerating voltage of 80 kV. All scale bars correspond to 1nm. (d) AC-TEM image showing detailed configurations of agglomerated S point defects into lines in different geometries, varying in length and width, which are marked by white circles and lines. The red and yellow ellipses show two line defect examples that both have two parallel S vacancy lines aggregated but in different lengths, which show a detectable variation on the lattice contraction level along the armchair direction. The scale bar corresponds to 0.5nm. (e-g) AC-TEM images of three typical examples of short 1SVL, 2SVL and 3SVL, respectively, which can be seen as the nucleation of extended line defects. All scale bars correspond to 0.5nm.

In figure 3 we examine the changes in bond reconstruction as a function of length for a 1SVL line defect in more detail. Figure 3a-3d are a series of AC-TEM images showing line defects of having only one line of single S vacancies (1SVL) but with lengths varying from 2 to 7 SVs (marked by white circles in figures 3a-d, respectively). Figure 3e shows the atomic model obtained from the DFT calculation in both the 2D projection (top down view) and side view based on figure 3d. A multislice image simulation based on the atomic model shown in figure 3e is presented in figure 3f and matches the experimental image. DFT calculations indicate that having the S vacancies all within the same layer reduces the energy by 1.7eV compared to random distribution across the two layers (supporting information figure S6). The formation of 1SVL alters the local stoichiometry from MoS_2 to Mo_3S_5, whereby the coordination of Mo atoms with S atoms at the defect site changes from six-fold to five-fold and S atoms maintain the three-fold coordination with Mo atoms as in a pristine lattice. The DFT calculated atomic model shows the generation of 1SVL triggers a slight out-of-plane distortion (side view), leading to the splitting of double stacked S atoms adjacent to 1SVL in the top down view (labelled by two black rectangular boxes in figure 3e). This results in the slight intensity decrease and blurring at the corresponding 2S sites in the AC-TEM image (marked in white square boxes in figure 3d). We measured the lattice contraction in 1SVL lines defects of different lengths by taking intensity line profiles along the armchair direction across the middle section (supporting information figure S7) spanning 2S-Mo_1-S-Mo_2, figure 3g (the subscripts are used to differentiate two Mo atoms measured in the same line). Comparing 1SVL with different lengths to the pristine lattice shows the projected atomic distances between 2S and Mo_1 are the same, figure 3g, whereas the distance between the two Mo atoms (Mo_1-Mo_2) has contracted, along with the S atom position moving closer to Mo_1 as the length of the 1SVL extends. We determined the projected atomic distances between Mo_1-S, S-Mo_2 and Mo_1-Mo_2 by Gaussian peak fitting, and figure 3h shows the plot of the relevant interatomic distances as a function of the 1SVL defect length. It shows that the Mo_1-Mo_2 distance has a compression that increases with the 1SVL length, from ~5.3 Å in a pristine lattice to ~4.2 Å when the aggregated number of S vacancies reaches 7 at 1SVL, yielding a shrinkage ratio of 21%. The planar Mo_1-S distance drastically decreases, while the S-Mo_2 distance increases when the aggregated number of single S vacancies increases from 0 to 5, indicating that a single S atom undergoes displacement relative to Mo_1 on its left. Therefore, with the extension of 1SVL, the projected view of the line defect structure shows an increased contraction ratio for Mo sublattice at 1SVL along the armchair direction, indicated by a continuous decrease of Mo_1–Mo_2 distance. In addition, residual single S atoms at 1SVL undergo displacement to Mo_1 atoms, which switches the original zigzag configuration of the Mo-S string to an approximately straight line (indicated by dashed rectangular black and white boxes in figure 3e and 3f, respectively).

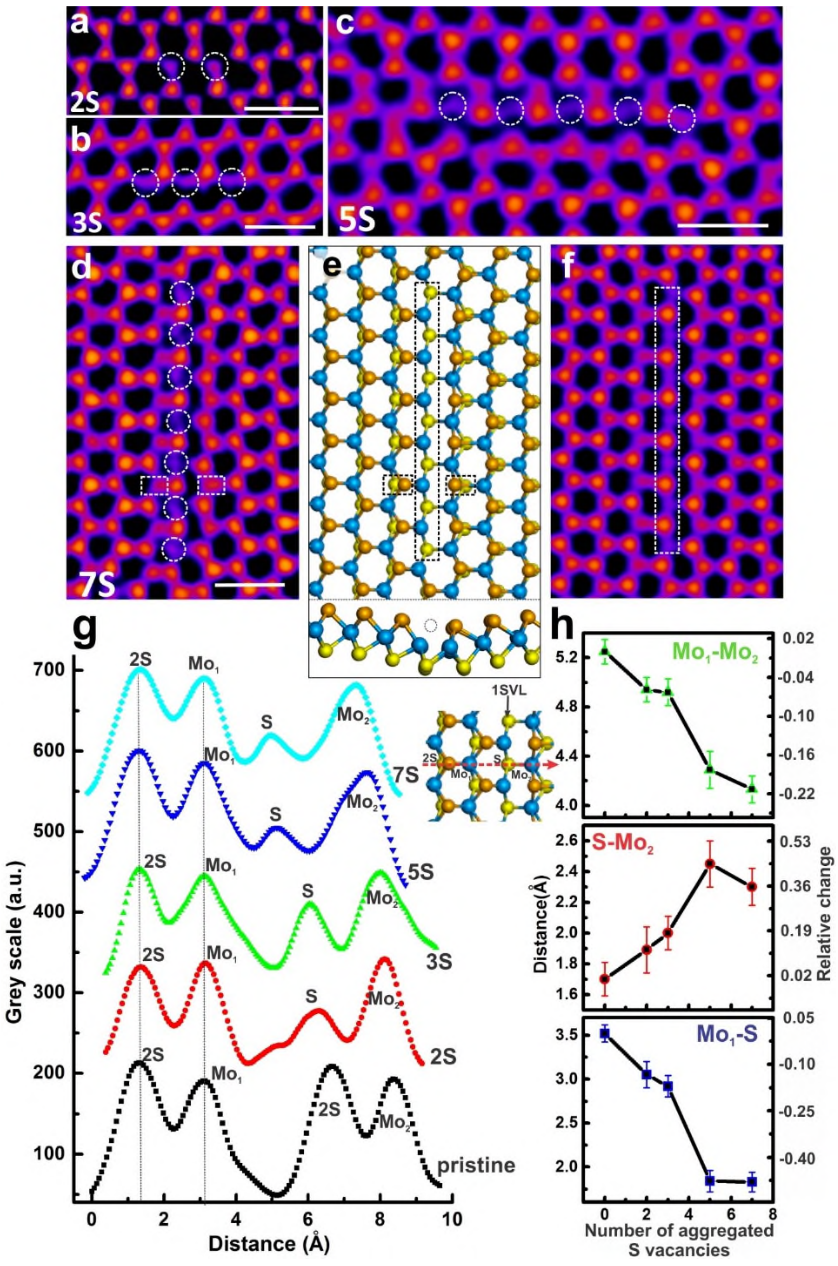

Figure 3. (a-d) AC-TEM images showing 1SVL in different lengths, having elevated numbers of single S vacancies aligning in the same line, being 2, 3, 5 and 7, respectively. (e) DFT-calculated atomic model based on figure 3d, with both the projection view and the associated side view. (f) Multislice TEM image simulation corresponding to the atomic model in figure 3e. (g) Intensity line profiles measured across the middle of 1SVL in different lengths, shown in figure 3a-3d, along the armchair direction indicated by the red arrow labelled in the schematic diagram, spanning 2S-Mo$_1$-S-Mo$_2$ in projection (the subscripts are used to differentiate two Mo atoms measured in the same line). (h) Scattered line graphs showing the distance variations between Mo$_1$ and Mo$_2$, S and Mo$_2$, as well as Mo$_1$ and S, respectively, when the number of aggregated single S vacancies increases from 0 to 7. Scale bar corresponds to 0.5nm in all panels.

We next studied the effect of increasing the width of line defects by examining the 2SVL that has two adjacent parallel sulphur vacancy lines. Figures 4a and 4b show two types of extended 2SVL defects, which have slightly different S reconstruction. Figure 4c shows a 2SVL with a kink that has the two different types of reconstruction present. The fine details of these reconstruction are shown in figure 4d-g, highlighting the shifts in the S positions and the impact on the positions of Mo along the line defect, figure 4h and 4i. The S atoms in the type 1 2SVL are further apart compared to the type 2 2SVL and the Mo atoms are spaced further apart in the type 1 2SVL compared to the type 2. Figure 4i shows the separation distances between Mo atoms along the regions indicated in the AC-TEM image in figure 4h, for type 1 and type 2 2SVL structures. The origin of the two types of 2SVL is likely associated with strain effects from the compression occurring in the lattice from the missing S atoms. The kink in the line defect in figure 4c results in non-orthogonal strain components from one line defect impacting on the other section. In general, type 1 2SVL is the most common 2SVL observed in the lattice.

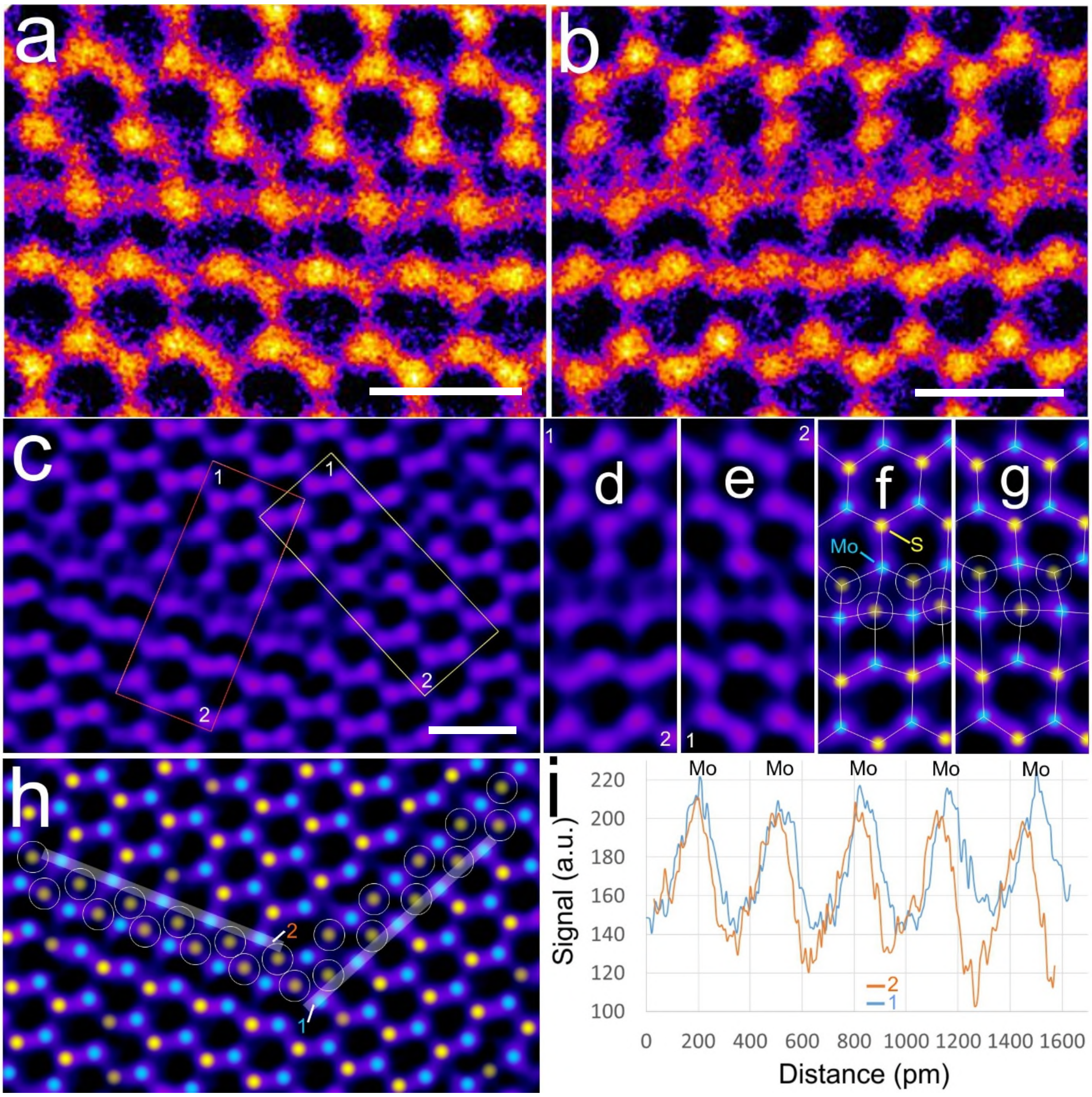

Figure 4. AC-TEM image of a 2SVL with (a) type 1 S reconstruction and (b) type 2 S reconstruction. (c) AC-TEM image showing the intersection of type 1 and type 2 2SVL defects. (d) Magnified view of the red boxed region in (c) for a type 2 2SVL. (e) Magnified view of the yellow boxed region in (c) for a type 1 2SVL. (f) and (g) show schematic atomic model overlaid onto the respective AC-TEM images from (d) and (e). (h) Positions of Mo and S atomic columns are indicated on the AC-TEM image from (c), with S in yellow and Mo in cyan. White circles indicate the S vacancy sites. (i) Comparison of line profiles taken in the regions indicated with the broad white lines in (h) for the two types of 2SVL. All scale bars corresponds to 0.5 nm.

Based on DFT calculations, the low energy configuration for the type 1 2SVL has alternating rows of S vacancies between top and bottom planes, shown in figure 5b, agreeing with previous reports.[29] Similar to 1SVL, 2SVL also induces a slight out-of-plane distortion at the defect site. The lowest coordination number of Mo atoms with S atoms further decreases from 5-fold for 1SVL to 3-fold for type 1 2SVL, figure 5b. The type 2 2SVL has similar S positions to a 1T phase of MoS_2 and in figure 5e-h we show it transformation to a type 1 2SVL structure after 10 seconds of electron beam irradiation. This occurs by shifting the single S atom line labelled in yellow circles (figure 5e) to right along the armchair direction slightly (figure 5h), switching the geometry of the Mo-S string on the right side from zigzag to a straight line. The type 2 2SVL usually occurs when there are other defect structures around, such as the triangular inversion domain shown in figure 5d. Figure 5i-l shows a schematic illustration of the atomic position changes needed to achieve a type 2 2SVL structure. The actual formation pathway of a type 2 2SVL will be more complicated than the process shown in figure 5i-l, because the line defects are formed by the agglomeration of point defects that involves multiple bond reconstructions.

The lattice changes for the 2SVL were measured as a function of their lengths and types using line profiles across the middle section spanning Mo_1-S-Mo_2, figure 5m. The short type 1 2SVL is from figure 2f, while the longer type 1 2SVL is from figure 5a (supporting information figure S8). The projected distances between Mo_1-Mo_2, S-Mo_1 and Mo_1-S in 2SVL as a function of their type and length are plotted in figure 5n. Compared with the pristine MoS_2 structure, both types of 2SVL have lattice compression along the armchair direction, as depicted in the line chart of Mo_1-Mo_2, figure 5n. However, the contraction for a type 1 2SVL (17%) is larger than for a type 2 (11%), even considering both the short type 1 2SVL and a long type 2 2SVL. The compression is greater for the longer type 1 2SVL compared to short type 1 2SVL, similar to 1SVL and confirms an increased lattice compression in the projected view with an extension of S vacancy lines. The position of single S atoms relative to its two neighbouring Mo atoms also varies for the two types of 2SVL. Compared with the pristine MoS_2 lattice having 2S placed closer to Mo_1, the single S atom tends to locate at approximately the middle of two Mo atoms for type 1 2SVL, whereas the type 2 2SVL has single S positioned closer to Mo_2.

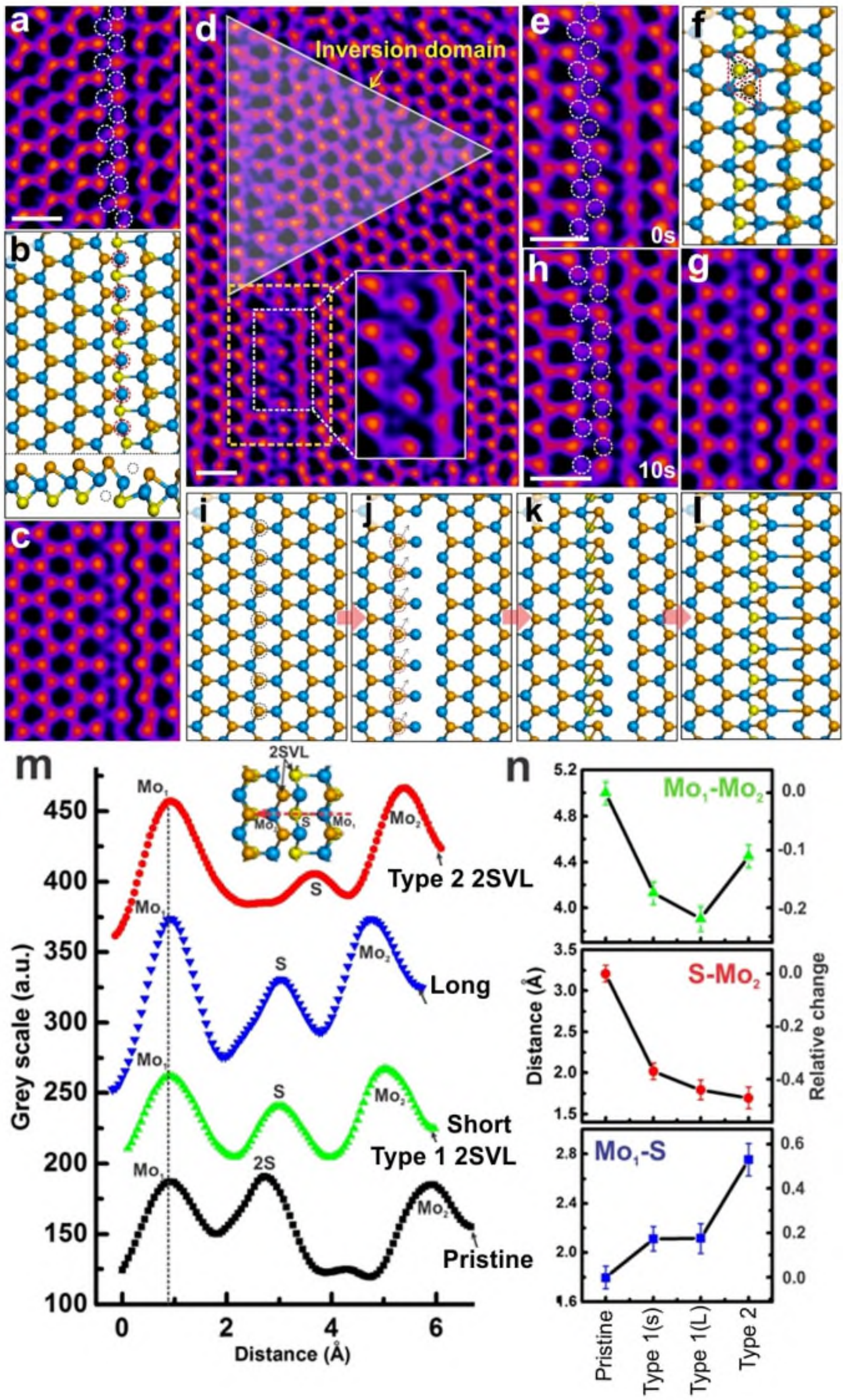

Figure 5. (a) AC-TEM image of type 1 2SVL with two adjacent single S vacancy lines highlighted by white circles. (b) DFT-calculated atomic model for the type 1 2SVL shown in figure 5a. The Mo atoms marked by red circles show a three-fold coordination with their neighbouring S atoms. (c) Multislice TEM image simulation based on the atomic model in figure 5b. (d) AC-TEM image showing type 2 2SVL with its surrounding environment included, having a triangular inversion domain on top. The detailed configuration of type 2 2SVL

labelled in the white dashed box is magnified as inset. (e) AC-TEM image of the region marked in the orange dashed box in figure 5d, with two single S vacancy lines marked by white and yellow circles from left to right, respectively. (f) Atomic model of type 2 2SVL, with labels indicating that single S atoms along two S vacancy lines are located in the centre of their triangularly-arranged three Mo atoms. (g) Multislice TEM image simulation based on the atomic model in figure 5f. (h) AC-TEM showing the transformation of a type 2 2SVL to type 1 after 10 seconds. (i-l) Schematic illustration showing atomic position changes from pristine lattice to type 2 2SVL. (m) Intensity line profiles measured across the middle of 2SVL in different types and lengths, along the armchair direction indicated by the red arrow shown in the schematic diagram. The short type 1 2SVL, long type 1 2SVL and type 2 2SVL correspond to the example of the type 1 2SVL in figures 2f, 5a and 5e, respectively. (n) Plots showing the distance difference between Mo_1 and Mo_2, S and Mo_2, as well as Mo_1-S, respectively, for 2SVL with the variation of types and lengths. Scale bar corresponds to 0.5nm in all panels.

The 2SVL further increases in width by S vacancies agglomerating along the armchair direction, forming 3SVL and 4SVL, as shown in figure 6a-c. These generally have structure similar to the type 1 2SVL in terms of the S bond reconstruction. Figure 6d shows the AC-TEM image of the region marked with the dashed white box in figure 6c, with the DFT-calculated relaxed atomic model and the corresponding multislice simulation shown in figure 6e and 6f, respectively. The energetically stable structure still has staggered arrangements of S line vacancies alternating between the top and bottom S planes, figure 6e. In the 2D projected view, the periodical structure at the defect site transforms from hexagonal in the pristine lattice to rectangular, highlighted by the red box in figure 6e. Intensity line profiles are measured for the 3SVLs with two different lengths (long and short) from images in figure 2g and 6d (figure 6g) (supporting information figure S9). Lattice contraction occurs along the armchair orientation and increases with the 3SVL length, agreeing with the observations on 1SVL and 2SVL. A prolonged electron beam irradiation causes the line defects to further expand in both length and width. Figures 6h and 6j are two typical examples of nSVL having 5 and 8 extended sulphur vacancy line widths, with corresponding atomic models shown in figures 6i and 6k, respectively. This indicates a large tunable range for line defect geometry, providing flexibility for patterning MoS_2-based 2D nanodevices.

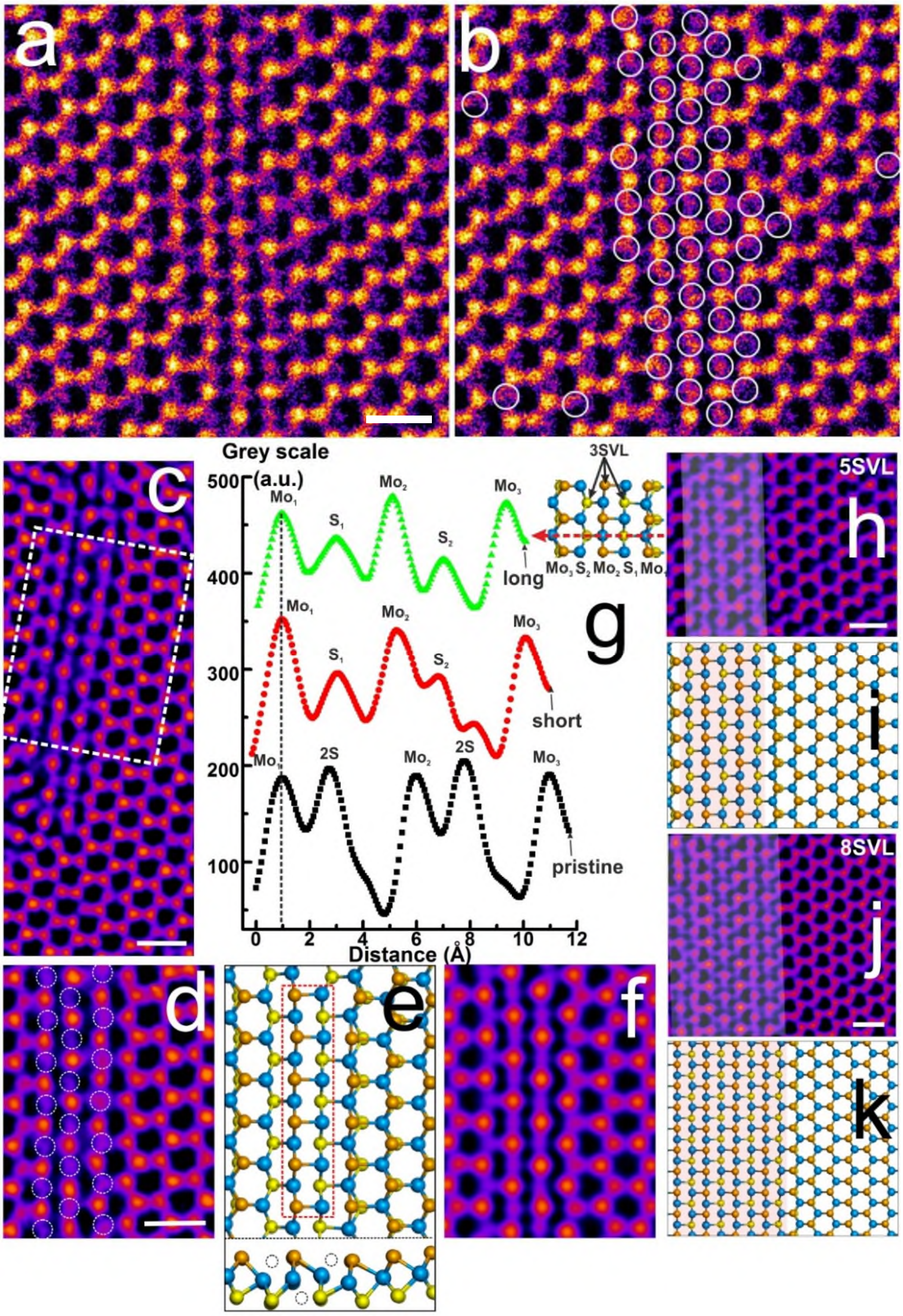

Figure 6. (a) AC-TEM image of S line vacancy with increased width, with (b) showing white circles to indicate the 1S vacancy locations. (c) AC-TEM image showing the structure of 3SVL. (d) Magnified AC-TEM image of the region labelled in the white dashed box in figure 6c, showing the detailed lattice reconstruction at 3SVL, with

three single S vacancy lines highlighted by white circles. (e) DFT-calculated atomic model of 3SVL corresponding to figure 6d. The lattice marked in the red dashed box indicates a transformation on the periodicity of atom arrangements from hexagons to rectangles in the projection view. (f) Multislice TEM image simulation based on the atomic model in figure 6e. (g) Intensity line profiles measured across the middle of 3SVL in different lengths, along the armchair direction indicated by the red arrow shown in the schematic diagram. The short and long examples correspond to 3SVL shown in figure 2g and figure 6d, respectively. (h, j) AC-TEM images showing two typical examples of nSVL (n>3), which are 5SVL and 8SVL, respectively. The line defect region has been highlighted by covering a half-transparent white mask, which displays distinct structural difference from the right pristine lattice with an atomically-sharp and straight boundary. (i, k) Atomistic models corresponding to the structure of 5SVL and 8SVL shown in figure 6h and 6j, respectively. Scale bar corresponds to 0.5nm in all panels.

We examine the strain in the lattice resulting from the line defect formation, figure 7. 2D displacement and strain maps were constructed for two typical examples of type 1 2SVL and 7SVL using a real space analysis method similar to prior work on carbon nanotubes.[31] Measuring changes in atomic positions has also been used to map strain in graphene grain boundaries and divacancies.[32,33] The 2D displacement maps of 2SVL and 7SVL show prominent lattice compression towards the line defects in the x direction with an increased magnitude as the line defect broadens (figure 7(i)a and 7(ii)a), whereas the lattice distortion in the y-axis is insignificant (figure 7(i)b and 7(ii)b) (supporting information figure S10). The compression or tension of the local lattice in the x-y plane is revealed by maps of $\frac{\partial U_x}{\partial x}$ and $\frac{\partial U_y}{\partial y}$. Interestingly, for type 1 2SVL, strain fields in the x direction are organized into tension-compression dipoles along the S line defects but in large magnitude variations, as indicated by black boxes in figure 7(i)c. The contraction strain fields can reach above 50%, while the tension strain fields are only around 20%. This is consistent with the atomic position measurements across the type 1 2SVL (figure 5n), where the projected interatomic distance of S-Mo_2 and Mo_1-S for the long type 1 2SVL show a compression and an elongation trend, respectively, with a distinct difference on the relative change. The strain field in the y direction is almost zero, which is due to the negligible displacement along this direction. Because the TEM image is the 2D projection of the 3D atomic structure, the elongation or shrinkage of the distance between two neighbouring atoms measured in a TEM image can come from two effects: (i) the bond length variation between two atoms, which indicates an in-plane lattice deformation; (ii) an out-of-plane distortion, which can alter the projected distance between two atoms along certain direction in the x-y plane. To confirm the origin of the 2D strain fields in the x direction in line defects, we calculated the Mo-S bond length variation between line defects in DFT-calculated atomic models and a pristine lattice, yielding a compression/tension ratio of less than 5% (supporting information figure S11). This indicates that both the contraction and tension fields along x-axis are mainly derived from the out-of-plane distortions of the lattice in line defects, also seen in the side view of atomic models for type 1 2SVL (figure 5b). The angle between Mo-S bonds and the x-y plane varies at the defect site compared with the pristine lattice, resulting in a change of the projected distance between Mo and S atoms. The 2D shear strain fields of $\frac{\partial U_x}{\partial y}$ are ordered into positive-negative dipoles as well (marked by black dashed boxes in figure 7(i)e), with an approximately balanced magnitude along the line defects, while $\frac{\partial U_x}{\partial y}$ is nearly ignorable, representing a periodically-organized simple shear mode in projection. Both the normal and shear strain fields are highly localized along the 2SVL, with small perturbations to the neighbouring lattice. In terms of strain field maps for 7SVL, they show similar characteristics as 2SVL regarding both the organization manner of strain fields and their magnitudes, as shown in figure 7(ii)c-f. The only difference is that the strain fields of $\frac{\partial U_x}{\partial x}$ along different S vacancy lines has small deviations in magnitudes, which could be due to the generation of ripples at line defects.

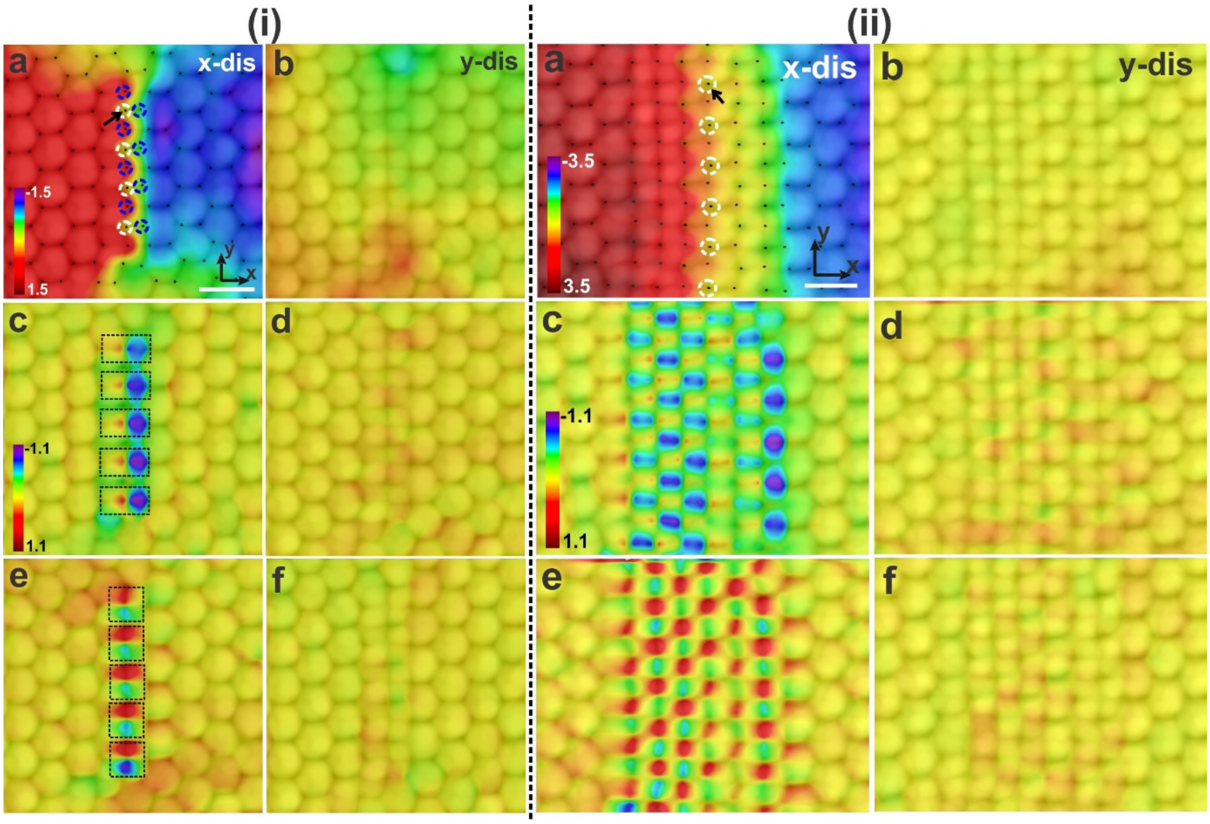

Figure 7. (i)(a, b) 2D displacement maps of type 1 2SVL in the x and y direction, respectively, which are overlaid on the corresponding maximum-filtered 2SVL AC-TEM image. The colour scale is ± 1.5Å. The white circles indicate the line of Mo atoms which locate close to its neighbouring two single S vacancy lines, marked by blue circles. The black arrow points out the Mo atom that is chosen as the reference point. (c-f) 2D strain maps of $\partial Ux/\partial x$, $\partial Uy/\partial y$, $\partial Ux/\partial y$ and $\partial Uy/\partial x$. The colour scale is ±1.1 (±110%). The black rectangular boxes marked in panel c show the normal strain fields in the x direction, which are organized into tension-compression dipoles with a large magnitude variation, while the black boxes labelled in panel e displays shear strain fields that are also ordered into pairs but with balanced magnitude along type 1 2SVL. (ii)(a, b) 2D displacement maps of 7SVL along the x and y direction, respectively, which are overlaid on the corresponding maximum-filtered 7SVL AC-TEM image. The colour scale is ± 3.5Å. The white circles indicate one line of Mo atoms which locates in the middle of the defective region. The black arrow indicates the Mo atom that is chosen as the reference point. (c-f) 2D strain maps of $\partial Ux/\partial x$, $\partial Uy/\partial y$, $\partial Ux/\partial y$ and $\partial Uy/\partial x$ for 7SVL. The colour scale is ±1.1 (±110%). Scale bar corresponds to 0.5nm in all panels.

Finally, we use DFT to calculate how the band structures of MoS_2 are impacted by the presence of these line defects. In particular, we study the electronic properties under the assumption of infinitely long line defects in MoS_2. For the band structure calculations, the infinite line defects are made within a periodic orthorhombic unit cell of the pristine MoS_2 lattice structure. As the width of the line defects increases, the size of the band gap decreases, as shown in figure 8. The band gap of pristine MoS_2 without a line defect is found to be 1.68 eV, similar to previous reports.[34,35] The defect lines introduce new states between the conduction band minimum and the valence band maximum, compared with the band structure of pristine MoS_2. The band structure of 1SVL, 2SVL, and 3SVL shows direct band gaps of 0.546, 0.058 eV, and 0.047 eV, respectively. As the number of defect lines increases over 4SVL, the band gap disappears and it finally becomes metallic (supporting information figure S12). From the band structure calculations, we find the tunability of band gap depending on the number of line defects.

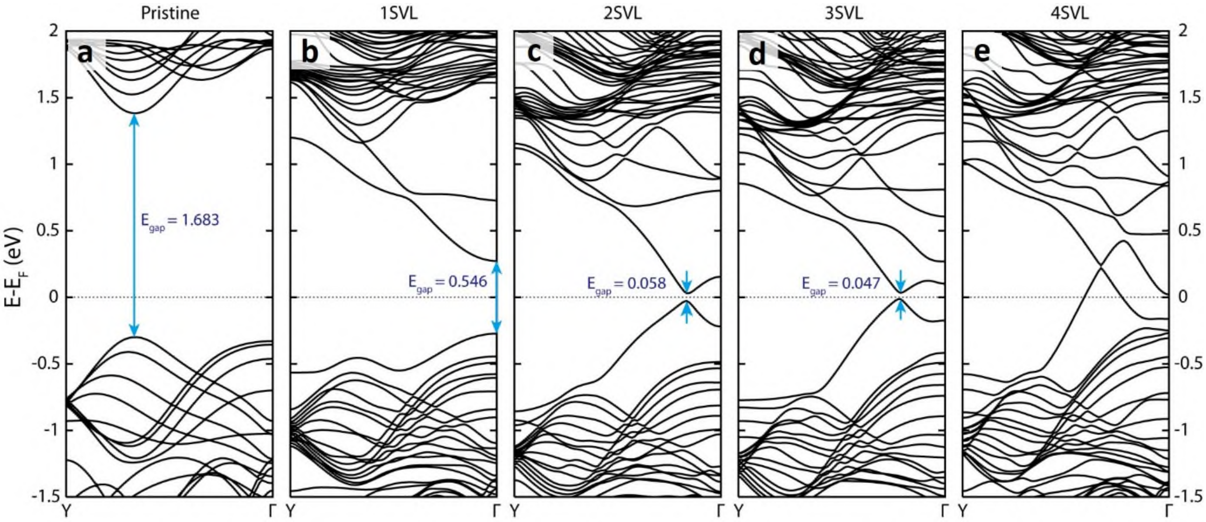

Figure 8. DFT calculated band structures of 1SVL, 2SVL, 3SVL and 4SVL, respectively, indicating a gradual band gap decrease as the line defect broadens with the electronic property alteration from semiconductor to metal.

Conclusion

The ability to accurately resolve the position of atoms within the defect structures in monolayer MoS_2 enabled precise atomic models to be constructed and verified by DFT. These refined models can be used to predict the properties of defective MoS_2 and have broad impact in understanding the role of lattice perturbations in 2D TMD materials. As the line defects increase in width, the DFT revealed a reduction in the band gap, eventually leading to metallic channels in the MoS_2. This opens up the opportunity for top-down patterning of semiconducting/metallic interfaces through defect engineering, which has importance for future electronic and opto-electronic devices.

Methods

Synthesis and transfer of monolayer MoS_2

MoS_2 monolayers were grown using a hydrogen-free chemical vapour deposition method in atmospheric pressure with precursors of molybdenum trioxide (MoO_3, ≥99.5%, Sigma-Aldrich) and sulphur (S, ≥99.5%, Sigma-Aldrich) powder, similar to a previously reported strategy. The MoO_3 monolayers were grown on the SiO_2/Si (300 nm thick SiO_2). To avoid the cross-contamination between MoO_3 and S powder at high temperature, MoO_3 precursor was initially loaded in a smaller diameter tube of around 1cm, which was then placed into the larger 1-inch quartz tube for the entire CVD growth, while the S powder was put in the outer tube. The mouth of the inner-tube which is located near the gas inlet was positioned upstream more than 15 cm from the position of S, which can thoroughly avoid the S vapour to spread into the inner-tube and react with MoO_3. Two furnaces were applied to provide a better temperature control for both precursors and the substrate. S powder and the substrate (with face up) were placed in the central area of the first and second furnace, respectively, while MoO_3 powder was loaded at the upstream of the second furnace. The heating temperature for S, MoO_3 and substrate were ~ 180, ~300, and ~800 °C with argon used as the carrier gas. After a pre-introduction of S vapour for ~15 min, the temperature for the second furnace was first increased to ~800 °C at a ramping rate of 40°C/min and maintained for 15 minutes under 150 sccm argon flow. Next, the argon flow was reduced to 10 sccm and kept for 25 minutes before the growth stopped, followed by a fast cooling process. The temperature for S was retained at ~180 ^{0}C during the whole synthesis period. After growth, the surface of the $MoS_2/SiO_2/Si$ substrate was first spin-coated with a thin film of poly (methyl methacrylate) (PMMA) followed by floating it on a 1 mol/L potassium hydroxide solution to etch SiO_2 away. After it peeled off, the PMMA/MoS_2 film was then transferred into the deionized water for several times to wash off any residual contamination from the etching process. The rinsed PMMA/MoS_2 film was subsequently scooped up by a holey Si_3N_4 TEM grid, (Agar Scientific Y5358), air-dried for overnight and baked at 180 ^{0}C for 15 minutes to ensure a strong interface contact between MoS_2 monolayers and the TEM grid. Finally, the PMMA scaffold was removed by submerging the TEM grid in the acetone solution for 8 hours.

Transmission electron microscopy and image processing

The HRTEM was conducted using Oxford's JEOL JEM-2200MCO field emission gun TEM with a CEOS imaging aberration corrector under an accelerating voltage of 80 kV. A double Wien filter monochromator with a 7 μm slit were applied to reduce the energy spread of the electron beam to ~0.21 eV. AC-TEM Images were recorded using a Gatan Ultrascan 4k × 4k CCD camera with 1-2 s acquisition time, 2 pixel binning. The pixel resolution for each AC-TEM image is 145 pixels/nm. The electron dose used for imaging was ~10^5 e^-/nm^2. Images were processed using the software of ImageJ. They were initially adjusted with a band-pass filter (between 100 and 1 pixel) to modify the long-range non-uniformity on the illumination intensity, and then smoothed by applying a Gaussian blur (2-4 pixels). The Gaussian blur applied on figures 2a-c is 8, which is for the specific purpose of highlighting locations of vacancies and line defects in the low magnification AC-TEM images. The original grayscale images with black atom contrast were inverted and then a fire false colour LUT was used to improve the visual contrast. Atomic models were established *via* the software of Accelrys

Discovery Studio Visualizer. Simulated multislice images based on corresponding atomic models were generated using JEMS software with a proper parameter adjustment according to the TEM experimental condition.

2D displacement maps and strain analysis

We identified the positions of atoms from the AC-TEM images having sulphur vacancy lines and subtracting them from their expected locations in a periodic pristine MoS_2 lattice. We used the approach previously applied to resolve the strain in carbon nanotubes. For 2D displacement maps, we rotated the TEM image to align the S vacancy line's length in the vertical direction (y-axis), and chose one set of Mo atoms as the reference point (indicated by the black arrow in the line of Mo atoms marked by white circles in figure 7(i)a and 7(ii)a, respectively). This is used to accurately align the corresponding Mo atom in a pristine lattice. The magnitude of each atom displacement is separately expressed by two directions, x and y. Atoms undergoing displacement to right (up) are in positive values, while those moving to left (down) are in negative. To resolve the 2D local lattice strain, we initially used scattered interpolation with a proper step-size on the displacement map, and then calculated the displacement value difference divided by their location variations along certain directions between each two interpolated spots to form 2D gradient maps of $\partial Ux/\partial x$, $\partial Uy/\partial y$, $\partial Ux/\partial y$ and $\partial Uy/\partial x$ (supporting information figures S13-S15).

Density Functional Theory (DFT) calculation

We performed DFT calculations within the generalized gradient approximation of Perdew-Burke-Ernzerhof (PBE) functional using Vienna *ab initio* simulation package (VASP) code.[36,37] Vanderbilt pseudopotentials are also used in this calculation.[38] To make the unit cell containing line defects, S atoms are pulled out depending on the number of SVL from the orthorhombic supercell containing 100 Mo atoms and 200 S atoms to make line defects. The size of supercell is determined considering the contraction by line defects observed in AC-TEM. In the unit cell, the vacuum region of 30 Å is contained in z direction. The basis set contains plane waves up to an energy cutoff of 400 eV. The Brillouin zone was sampled using only Γ point. When structural relaxations are performed, the structure is relaxed under the constraint until the force on each atom is smaller than 0.02 eV/Å. For the band structure calculations, the infinite line defects are made in the periodic orthorhombic unit cell (44.063 Å×3.180 Å×30 Å) of the pristine MoS_2 lattice structure containing 16 Mo atoms and 32 S atoms. The infinite line defects are formed along y-direction. In the band structure calculations, the Brillouin zone was sampled using a (1×13×1) Γ-centered mesh.

Conflict of Interest: The authors declare no competing financial interest.

Acknowledgements

JHW thanks the Royal Society for support. SW thanks the China Scholarship Council for support. G.-D.L. acknowledges support from the Supercomputing Center/Korea Institute of Science and Technology Information with supercomputing resources (KSC-2015-C3-011), from the BK21 plus program, and from the National Research Foundation of Korea (NRF) grant funded by the Korea government (RIAM No. 2010-0012670).

Supporting Information Available: Supplementary figures including AC-TEM images in the grayscale of SV and DV, bond length measurements on the DFT-calculated atomic model of SV and DV, the atomic model illustrating one possible structure of 1SVL with single S atoms having up-down-up-down configuration, the detailed locations of taking intensity line profiles on 1SVL, 2SVL and 3SVL, the raw AC-TEM images for 2D displacement and strain maps, and the DFT-calculated band structures of line defects from 5SVL to 8SVL. This material is available free of charge *via* the Internet at http://pubs.acs.org.

References

(1) Radisavljevic, B.; Radenovic, A.; Brivio, J.; Giacometti, V.; Kis, A. Single-Layer MoS_2 Transistors. *Nat. Nanotechnol.* **2011**, *6*, 147–150.

(2) Wang, Q. H.; Kalantar-Zadeh, K.; Kis, A.; Coleman, J. N.; Strano, M. S. Electronics and Optoelectronics of Two-Dimensional Transition Metal Dichalcogenides. *Nat. Nanotechnol.* **2012**, *7*, 699–712.

(3) Ganatra, R.; Zhang, Q. Few Layer MoS_2 - A Promising Layered Semiconductor. *ACS Nano* **2014,** *8*, 4074–4099.

(4) Amani, M.; Chin, M. L.; Birdwell, A. G.; O'Regan, T. P.; Najmaei, S.; Liu, Z.; Ajayan, P. M.; Lou, J.; Dubey, M. Electrical Performance of Monolayer MoS_2 Field-Effect Transistors Prepared by Chemical Vapor Deposition. *Appl. Phys. Lett.* **2013**, *102*, 193107.

(5) Zhou, K.-G.; Mao, N.-N.; Wang, H.-X.; Peng, Y.; Zhang, H.-L. A Mixed-Solvent Strategy for Efficient Exfoliation of Inorganic Graphene Analogues. *Angew. Chem. Int. Ed. Engl.* **2011**, *50*, 10839–10842.

(6) Dunne, P. W.; Munn, A. S.; Starkey, C. L.; Lester, E. H. The Sequential Continuous-Flow Hydrothermal Synthesis of Molybdenum Disulphide. *Chem. Commun.* **2015**, *51*, 4048–4050.

(7) Zhan, Y.; Liu, Z.; Najmaei, S.; Ajayan, P. M.; Lou, J. Large-Area Vapor-Phase Growth and Characterization of MoS_2 Atomic Layers on a SiO_2 Substrate. *Small* **2012**, *8*, 966–971.

(8) Liu, K.-K.; Zhang, W.; Lee, Y.-H.; Lin, Y.-C.; Chang, M.-T.; Su, C.-Y.; Chang, C.-S.; Li, H.; Shi, Y.; Zhang, H.; Lai, C.-S.; Li, L.-J. Growth of Large-Area and Highly Crystalline MoS_2 Thin Layers on Insulating Substrates. *Nano Lett.* **2012**, *12*, 1538–1544.

(9) van der Zande, A. M.; Huang, P. Y.; Chenet, D. A.; Berkelbach, T. C.; You, Y.; Lee, G.-H.; Heinz, T. F.; Reichman, D. R.; Muller, D. A.; Hone, J. C. Grains and Grain Boundaries in Highly Crystalline Monolayer Molybdenum Disulphide. *Nat. Mater.* **2013**, *12*, 554–561.

(10) Najmaei, S.; Liu, Z.; Zhou, W.; Zou, X.; Shi, G.; Lei, S.; Yakobson, B. I.; Idrobo, J.-C.; Ajayan, P. M.; Lou, J. Vapour Phase Growth and Grain Boundary Structure of Molybdenum Disulphide Atomic Layers. *Nat. Mater.* **2013**, *12*, 754–759.

(11) Wang, S.; Rong, Y.; Fan, Y.; Pacios, M.; Bhaskaran, H.; He, K.; Warner, J. H. Shape Evolution of Monolayer MoS_2 Crystals Grown by Chemical Vapor Deposition. *Chem. Mater.* **2014**, *26*, 6371–6379.

(12) Yu, Y.; Li, C.; Liu, Y.; Su, L.; Zhang, Y.; Cao, L. Controlled Scalable Synthesis of Uniform, High-Quality Monolayer and Few-Layer MoS_2 Films. *Sci. Rep.* **2013**, *3*, 1866.

(13) Kang, K.; Xie, S.; Huang, L.; Han, Y.; Huang, P. Y.; Mak, K. F.; Kim, C.-J.; Muller, D.; Park, J. High-Mobility Three-Atom-Thick Semiconducting Films with Wafer-Scale Homogeneity. *Nature* **2015**, *520*, 656–660.

(14) Mouri, S.; Miyauchi, Y.; Matsuda, K. Tunable Photoluminescence of Monolayer MoS2 *via* Chemical Doping. *Nano Lett.* **2013**, *13*, 5944–5948.

(15) Sim, D. M.; Kim, M.; Yim, S.; Choi, M.-J.; Choi, J.; Yoo, S.; Jung, Y. S. Controlled Doping of Vacancy-Containing Few-Layer MoS_2 *via* Highly Stable Thiol-Based Molecular Chemisorption. *ACS Nano* **2015**, *9*, 12115–12123.

(16) Conley, H. J.; Wang, B.; Ziegler, J. I.; Haglund, R. F.; Pantelides, S. T.; Bolotin, K. I. Bandgap Engineering of Strained Monolayer and Bilayer MoS_2. *Nano Lett.* **2013**, *13*, 3626–3630.

(17) Desai, S. B.; Seol, G.; Kang, J. S.; Fang, H.; Battaglia, C.; Kapadia, R.; Ager, J. W.; Guo, J.; Javey, A. Strain-Induced Indirect to Direct Bandgap Transition in Multilayer WSe_2. *Nano Lett.* **2014,** *14*, 4592–4597.

(18) Lin, Y.-C.; Dumcenco, D. O.; Huang, Y.-S.; Suenaga, K. Atomic Mechanism of the Semiconducting-to-Metallic Phase Transition in Single-Layered MoS_2. *Nat. Nanotechnol.* **2014**, *9*, 391–396.

(19) Banhart, F.; Kotakoski, J.; Krasheninnikov, A. V. Structural Defects in Graphene. *ACS Nano* **2011**, *5*, 26–41.

(20) Liu, L.; Qing, M.; Wang, Y.; Chen, S. Defects in Graphene: Generation, Healing, and Their Effects on the Properties of Graphene: A Review. *J. Mater. Sci. Technol.* **2015**, *31*, 599–606.

(21) Lin, Y. – C.; Bjorkman, T.; Komsa, H. – P.; Teng, P. Y.; Yeh, C. H.; Huang, F. S.; Lin, K. – H.; Jadczak, J.; Huang, Y. – S.; Chiu, P. – W.Three-Fold Rotational Defects in Two-Dimensional Transition Metal Dichalcogenides. *Nat. Commun.* **2015**, *6*, 6736.

(22) Zhou, W.; Zou, X.; Najmaei, S.; Liu, Z.; Shi, Y.; Kong, J.; Lou, J.; Ajayan, P. M.; Yakobson, B. I.; Idrobo, J.-C. Intrinsic Structural Defects in Monolayer Molybdenum Disulfide. *Nano Lett.* **2013,** *13*, 2615–2622.

(23) Azizi, A.; Zou, X.; Ercius, P.; Zhang, Z.; Elías, A. L.; Perea-López, N.; Stone, G.; Terrones, M.; Yakobson, B. I.; Alem, N. Dislocation Motion and Grain Boundary Migration in Two-Dimensional Tungsten Disulphide. *Nat. Commun.* **2014**, *5*, 4867.

(24) Börrnert, F.; Fu, L.; Gorantla, S.; Knupfer, M.; Büchner, B.; Rümmeli, M. H. Programmable Sub-Nanometer Sculpting of Graphene with Electron Beams. *ACS Nano* **2012**, *6*, 10327–10334.

(25) Robertson, A. W.; Allen, C. S.; Wu, Y. A.; He, K.; Olivier, J.; Neethling, J.; Kirkland, A. I.; Warner, J. H. Spatial Control of Defect Creation in Graphene at the Nanoscale. *Nat. Commun.* **2012**, *3*, 1144.

(26) Lin, J.; Pantelides, S. T.; Zhou, W. Vacancy-Induced Formation and Growth of Inversion Domains in Transition-Metal Dichalcogenide Monolayer. *ACS Nano* **2015**, *9*, 5189–5197.

(27) Komsa, H.-P.; Kotakoski, J.; Kurasch, S.; Lehtinen, O.; Kaiser, U.; Krasheninnikov, A. V. Two-Dimensional Transition Metal Dichalcogenides under Electron Irradiation: Defect Production and Doping. *Phys. Rev. Lett.* **2012**, *109*, 035503.

(28) Zan, R.; Ramasse, Q. M.; Jalil, R.; Georgiou, T.; Bangert, U.; Novoselov, K. S. Control of Radiation Damage in MoS_2 by Graphene Encapsulation. *ACS Nano* **2013**, *7*, 10167–10174.

(29) Komsa, H.-P.; Kurasch, S.; Lehtinen, O.; Kaiser, U.; Krasheninnikov, A. V. From Point to Extended Defects in Two-Dimensional MoS_2: Evolution of Atomic Structure under Electron Irradiation. *Phys. Rev. B* **2013**, *88*, 035301.

(30) Liu, H.; Jiao, L.; Yang, F.; Cai, Y.; Wu, X.; Ho, W.; Gao, C.; Jia, J.; Wang, N.; Fan, H.; Yao, W.; Xie, M. Dense Network of One-Dimensional Midgap Metallic Modes in Monolayer $MoSe_2$ and Their Spatial Undulations. *Phys. Rev. Lett.* **2014**, *113*, 066105.

(31) Warner, J. H.; Young, N. P.; Kirkland, A. I.; Briggs, G. A. D. Resolving Strain in Carbon Nanotubes at the Atomic Level. *Nat. Mater.* **2011**, *10*, 958–962.

(32) Rasool, H. I.; Ophus, C.; Zhang, Z.; Crommie, M. F.; Yakobson, B. I.; Zettl, A. Conserved Atomic Bonding Sequences and Strain Organization of Graphene Grain Boundaries. *Nano Lett.* **2014,** *14*, 7057–7063.

(33) Chen, Q.; Robertson, A. W.; He, K.; Gong, C.; Yoon, E.; Lee, G-D.; Warner, J. H.; Atomic Level Distributed Strain within Graphene Divacancies from Bond Rotations, *ACS Nano*, **2015**, 9, 8599-8608

(34) Lebègue, S.; Eriksson, O. Electronic Structure of Two-Dimensional Crystals from *Ab Initio* Theory. *Phys. Rev. B* **2009**, *79*, 115409.

(35) Bhattacharyya, S.; Singh, A. K. Semiconductor-Metal Transition in Semiconducting Bilayer Sheets of Transition-Metal Dichalcogenides. *Phys. Rev. B* **2012**, *86*, 075454.

(36) Perdew, J. P.; Burke, K.; Ernzerhof, M. Generalized Gradient Approximation Made Simple. *Phys. Rev. Lett.* **1996**, *77*, 3865–3868.

(37) Kresse, G.; Furthmüller, J. Efficient Iterative Schemes for *Ab Initio* Total-Energy Calculations Using a Plane-Wave Basis Set. *Phys. Rev. B* **1996**, *54*, 11169–11186.

(38) Vanderbilt, D. Soft Self-Consistent Pseudopotentials in a Generalized Eigenvalue Formalism. *Phys. Rev. B* **1990**, *41*, 7892–7895.

TOC graphic